Distribution Category
UC-92a

LAWRENCE LIVERMORE LABORATORY
University of California/Livermore, California/94550

UCRL-50036-78-4

LLL GAS STIMULATION PROGRAM QUARTERLY PROGRESS REPORT OCTOBER THROUGH DECEMBER 1978

M. E. Hanson, G. D. Anderson, R. J. Shaffer, D. N. Montan, L. D. Thorson, W. Lin, B. C. Haimson*, and M. P. Cleary†

MS. date: February 7, 1979

*University of Wisconsin, Madison, Wisconsin.
†Massachusetts Institute of Technology, Cambridge, Massachusetts.

PREFACE

Although U. S. gas resources remain large, proven reserves have declined to 230 trillion feet, and the current reserves/production ratio is 10 to 1.

It is estimated that tight (i.e., low-permeability), western gas reservoirs and eastern Devonian gas shales contain large quantities of natural gas, but because of the low permeability, these resources have been difficult to recover. Some gas has been produced, but industry needs more economical recovery techniques. The region around the production wells must be stimulated in some manner to induce a more rapid flow into the well bore. The stimulation process involves creating channels or cracks out into the reservoir from the well bore. This can be done by detonating high explosives or nuclear explosives in the well bore or by hydraulically fracturing the formation.

Currently, the most promising techniques for stimulating low-permeability gas reservoirs are hydraulic fracturing and massive hydraulic fracturing (MHF). Hydraulic fracturing involves pumping fluids under high pressure down the well bore and out into the reservoir. The hydraulic action fractures the rock around the well bore, and proppants in the fracturing fluids hold the cracks open. The fractures provide large drainage faces for the gas and channel it into the well bore. Hydraulic fracturing has been routinely used in oil-well completion and cleanup for many years. MHF differs from hydraulic fracturing in that larger amounts of fluid and proppant are pumped down the well to create and prop fractures at much greater distances.

The application of MHF techniques to tight western gas formations has given variable and sometimes disappointing results. The best efforts of a CER-led industry/government consortium to stimulate the Piceance Basin near Rio Blanco, Colorado, were not successful. On the other hand, Amoco has used MHF techniques in the Wattenburg field near Denver with a high degree of success. Significant differences in the reservoirs themselves apparently account for the differences in success.

The Devonian shales present similar problems. It is believed that production from these gas shales results from the connection of the wells to the existing fracture patterns. Hence, to recover this gas, we must locate the producing zones, locate the natural fractures near the well bore, and fracture from the well bore to the existing fractures.

The Lawrence Livermore Laboratory (LLL) has embarked on a research program to help develop tight gas reservoirs in the United States. We are trying to obtain a more detailed understanding of the stimulation processes, including how the formation properties interact with and affect these processes. The problem is to determine how to connect the maximum amount of productive reservoir rock to the well bore through a highly permeable fracture system.

There are several questions that we would like to be able to answer in advance about the tight Rocky Mountain formations. Can we identify particular sections where the fractures may be expected to be preferentially confined to the productive sands, so that a maximum volume of reservoir can be stimulated? What is the geometry (length, width, and number) of the fractures? What is the nature of the treatment (fluid composition, volumes, pumping rates, perforation intervals) which, when applied to a formation with certain properties, will result in optimum and economical recovery? What are some of the important geophysical measurements and experiments that can aid in this endeavor? What data and experiences exist that are relevant? Most of the western reservoirs contain a high degree of water saturation, which can significantly reduce the already low permeability of these reservoirs; is it possible to use existing logging techniques supplemented by new geophysical measurements to ascertain the *in situ* water saturation?

Devonian shales present many of the same challenges as the tight Rocky Mountain formations. There are, however, some special problems. Logging techniques for these shales are just being developed, and we have not yet acquired the ability to locate the fractures that do not intersect the well bore. The effect of hydraulic fracturing on Devonian shales is also not well understood. Water, one of the standard hydraulic fracturing fluids, can cause significant formation damage; organic and cryogenic fluids are expensive; high-explosive fracturing makes well clean-out and completion costly and uncertain; and, as we have shown previously,[1] the diameter of permeability enhancement is small.

Our program is primarily investigative. We are not currently proposing any field programs. We are, however, constructing and applying theoretical models and performing laboratory experiments to develop an understanding of the gas stimulation process. These tasks are complementary, and parallel development is

We have completed a series of calculations evaluating the strain field near an interface caused by the proximity of a hydraulically inflated fracture.* These calculations differ from those presented in our previous Quarterly Report[6] in that the Young's moduli on both sides of the interface are identical, but the Poisson's ratio differs across the interface. We assume the medium around the cracks to be impermeable and the pressure in the crack to be constant. We performed two sets of calculations, one having the smaller Poisson's ratio in the material surrounding the crack and a larger Poisson's ratio in the material on the other side of the interface (Fig. 1), and the other with the Poisson's ratio interchanged with respect to the first set. Figure 1 shows the geometry of the problem. The two dimensionless coordinates ξ and η have been normalized with respect to the crack length.

We have calculated and plotted the strain normal to the interface and the shear strain along the interface for several positions of the crack with respect to the interface (Figs. 2 through 9). We computed shear strain values along the interface. Because we used a finite-element numerical model to calculate the elastic field, the strain values were computed on either side of the interface. Each curve on these plots is for a crack at one distance ξ from the interface. In these calculations, the Young's modulus E was equal to 10 GPa and was constant on both sides of the interface; Poisson's ratio was varied across the interface. The pressure in the crack was 30 MPa, and the calculations were performed in plane strain. Figures 2 through 5 show the normal and shear strain values for the case where $\nu_1 = 0.15$ and $\nu_2 = 0.35$. Figures 2 and 3 show the normal and shear strain just to the left of the interface; the strain values adjacent to the interface on the right are shown in Figs. 4 and 5. We see that the normal strain becomes more compressive as the crack tip nears the interface. In addition, the position of maximum compression moves toward the extended axis of the fracture as the tip approaches the interface. We also note that, for this case, the most compressive normal stress along the interface occurs on the side opposite the fractures in the material with the larger Poisson's ratio. However, the tensile normal strain just ahead of the fracture tip increases as the fracture approaches the interface and remains larger in the material to the left of the interface.

The shear strains for this case increase as the fracture tip approaches the interface. We also note that the maximum shear strain moves toward the fracture axis as the fracture tip approaches the interface. However, the larger shear does not approach the line $\eta = 0$ (this line extends along the fracture axis to the interface) as rapidly in the larger Poisson's ratio material.

Figures 6 through 9 show the case where the fracture is embedded in the material with the larger Poisson's ratio. Figures 6 and 7 show the strain values just to the left of the interface, and Figs. 8 and 9 display the strain values on the right side of the interface. Here we note that the maximum compressive stress occurs to the left of the interface in the material with the larger Poisson's ratio. However, the tensile strain directly ahead of the crack increases in the material across the interface where Poisson's ratio is smaller. The characteristic of the maximum compression increasing and moving toward the extended fracture axis is similar to the previous case; however, we note that the position of maximum compression is spaced somewhat further from the fracture axis.

We have performed these calculations without a compression on the field (e.g., without effects from an *in situ* stress) to reduce computing time requirements. It is obvious that if the strain energy were transported across the interface by friction (e.g., under compression with a frictional coefficient), the tension resulting in the top region could reduce the frictional stresses in that area. This could significantly affect the transport of strain energy across a "frictional" interface, as well as propagation across the interface.

EFFECTS OF EXISTING CRACKS NEAR INTERFACES

We have analyzed the characteristics of a constant-length, quasi-static fracture approaching and penetrating a well bonded interface between two materials. The materials are simulated by a difference in the Young's modulus across the interface. We presented results for this case in the two previous Quarterly Reports[5,6] indicating that the influence of the material on the other side of the interface considerably affects the stress-intensity factor at each crack tip. We also noted that when the fracture is contained in the smaller modulus material and is quasi-statically approaching the higher modulus material, the stress-intensity factor is seen to decrease significantly

*We are performing these calculations to develop an understanding of the changes in strain as a result of the presence of a pressurized fracture, and to form a base case for the analysis of frictional effects along the interface.

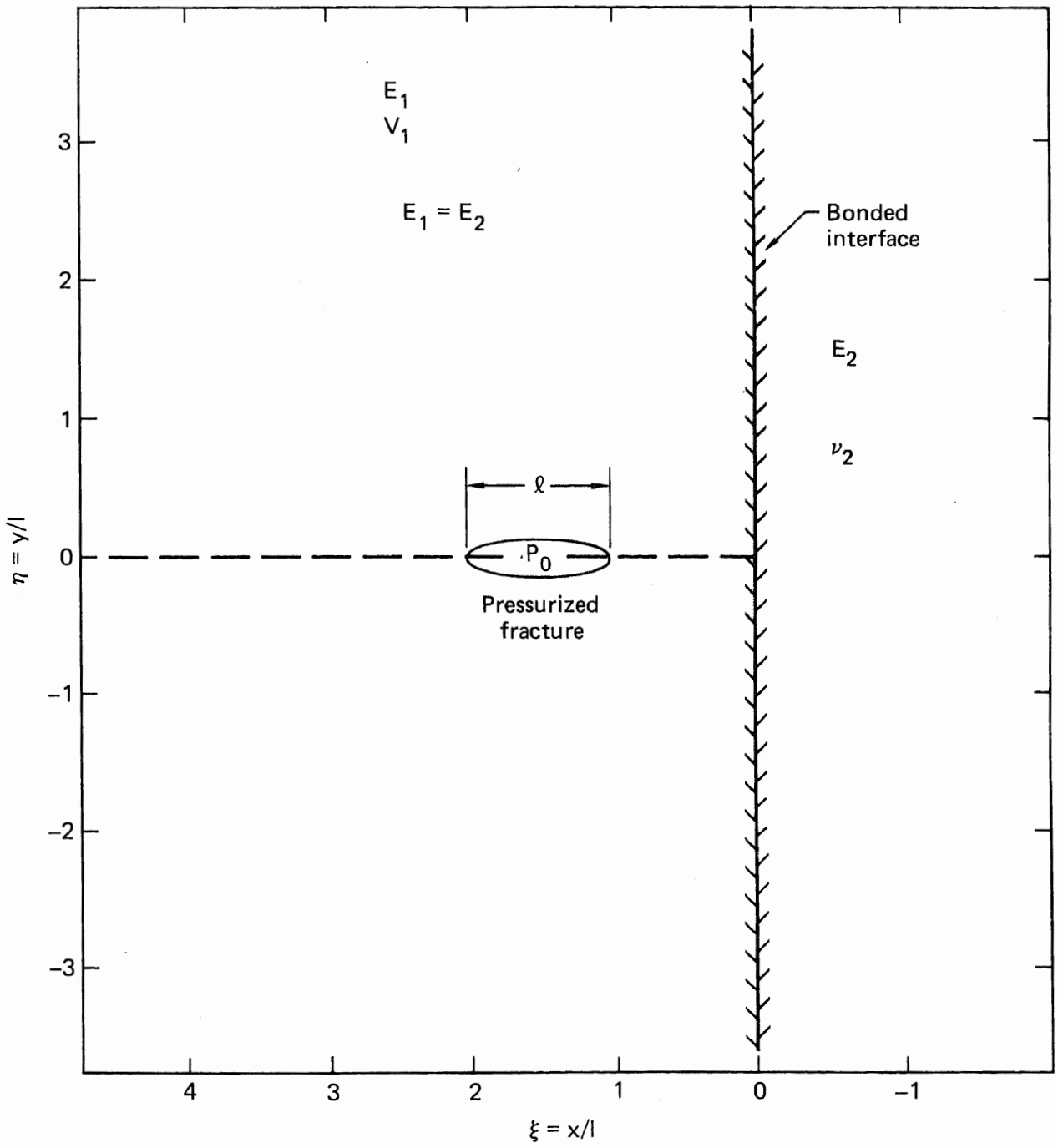

Fig. 1. Geometry of problems with cracks approaching bonded interface between two materials having material moduli E_1, ν_1 and E_2, ν_2.

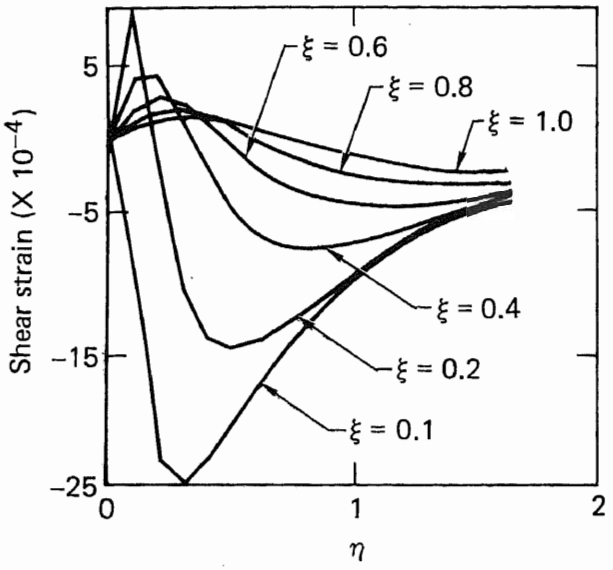

Fig. 2. Shear strain to left of interface as a function of distance along the interface for various distances of the fracture tip from the interface, $\frac{P_0}{E_1} = \frac{P_0}{E_2} = 3 \times 10^{-3}$, $\nu_1 = 0.15$, $\nu_2 = 0.35$.

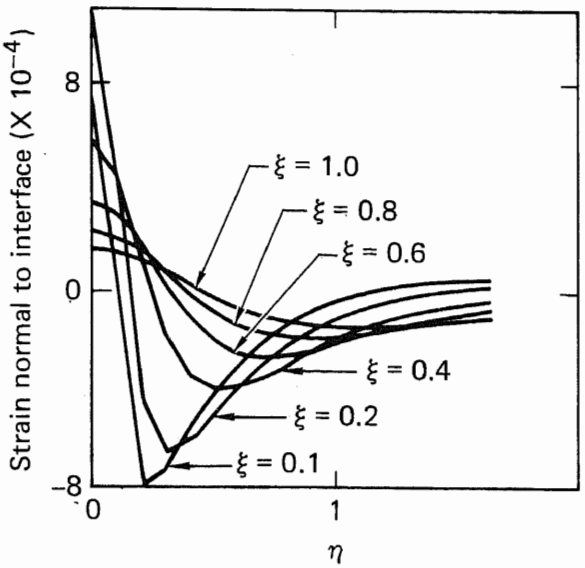

Fig. 3. Normal strain to the left of the interface as a function of distance along the interface for various fracture tip distances from the interface, $\frac{P_0}{E_1} = \frac{P_0}{E_2} = 3 \times 10^{-3}$, $\nu_1 = 0.15$, $\nu_2 = 0.35$.

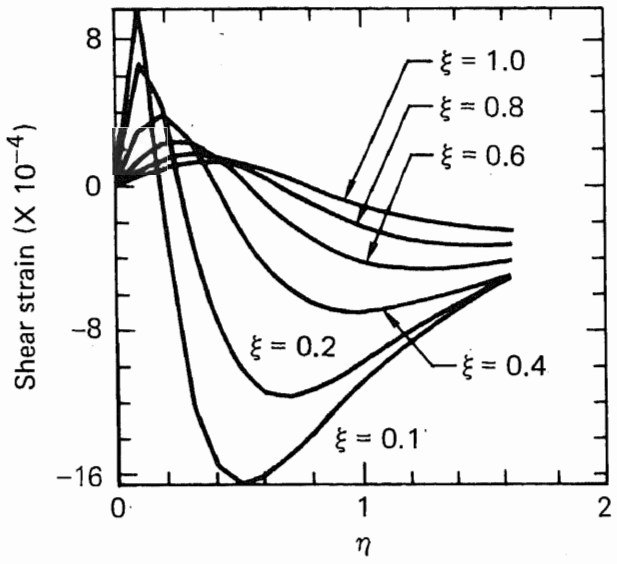

Fig. 4. Shear strain to the right of the interface as a function of distance along the interface for various distances of the fracture tip from the interface, $\frac{P_0}{E_1} = \frac{P_0}{E_2} = 3 \times 10^{-3}$, $\nu_1 = 0.15$, $\nu_2 = 0.35$.

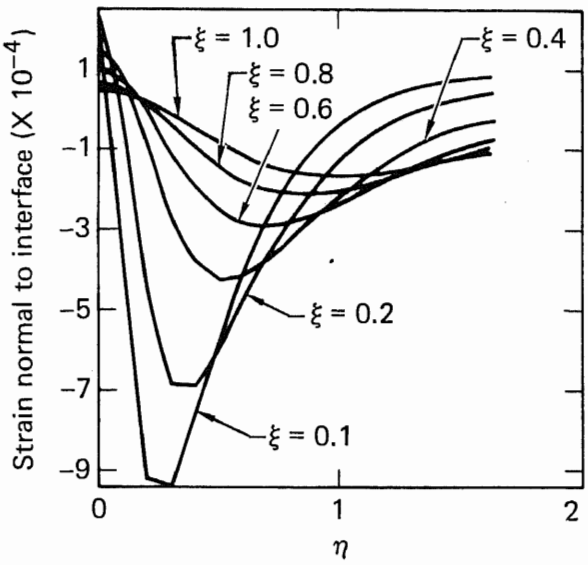

Fig. 5. Shear strain to the right of the interface as a function of distance along the interface for various fracture tip distances from the interfaces, $\frac{P_0}{E_1} = \frac{P_0}{E_2} = 3 \times 10^{-3}$, $\nu_1 = 0.15$, $\nu_2 = 0.35$.

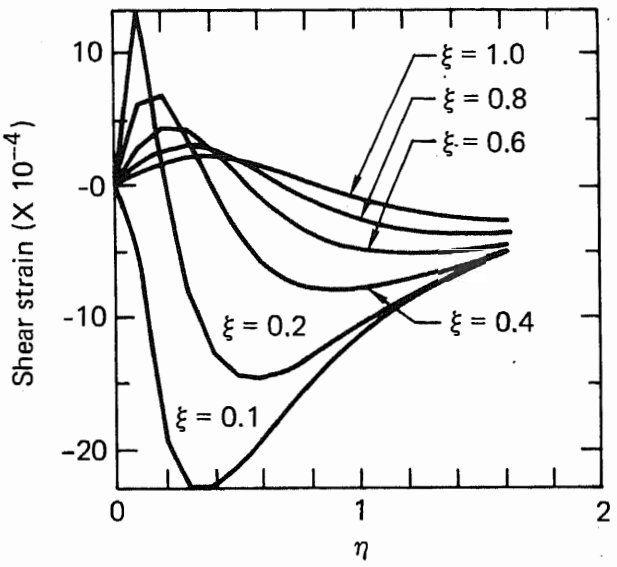

Fig. 6. Shear strain to the left of the interface as a function of distance along the interface for various fracture tip distances from the interface, $\frac{P_0}{E_1} = \frac{P_0}{E_2} = 3 \times 10^{-3}$ and $\nu_1 = 0.35$, $\nu_2 = 0.15$.

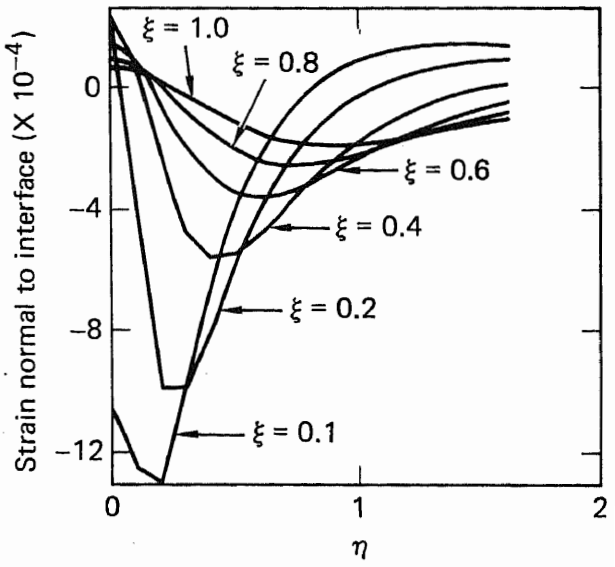

Fig. 7. Normal strain to the left of the interface as a function of distance along the interface for various fracture tip distances from the interface, $\frac{P_0}{E_1} = \frac{P_0}{E_2} = 3 \times 10^{-3}$, $\nu_1 = 0.35$, $\nu_2 = 0.15$.

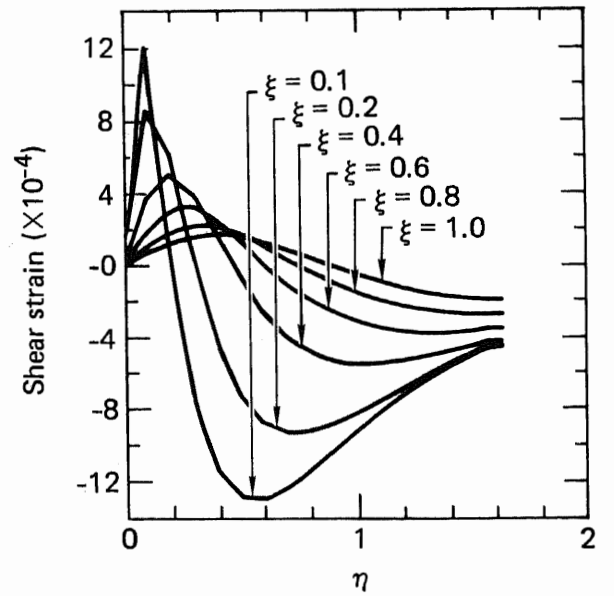

Fig. 8. Shear strain to the right of the interface as a function of distance along the interface for various fracture tip distances from the interface, $\frac{P_0}{E_1} = \frac{P_0}{E_2} = 3 \times 10^{-3}$, $\nu_1 = 0.35$, $\nu_2 = 0.15$.

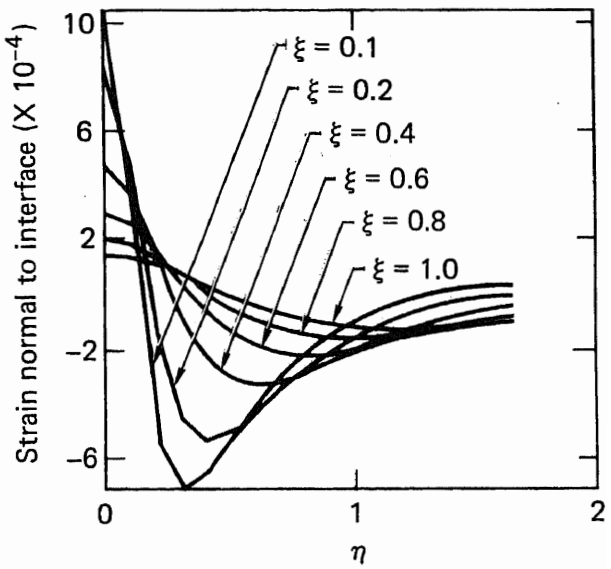

Fig. 9. Normal strain to the right of the interface as a function of distance along the interface for various fracture tip distances from the interface, $\frac{P_0}{E_1} = \frac{P_0}{E_2} = 3 \times 10^{-3}$, $\nu_1 = 0.35$, $\nu_2 = 0.15$.

as the tip approaches the interface. However, as the leading crack tip penetrates the interface and enters the higher modulus material we see that its stress-intensity factor increases to a value larger than that for a homogeneous material with this higher modulus. Our calculations also predict that the stress-intensity factor at the opposite crack tip in the lower modulus material decreases.

We have completed some calculations to assess how existing fractures in the higher modulus material affect the stress-intensity factor as the pressurized fracture approaches the interface (we have not performed the calculations for the case when the pressurized crack penetrates the interface). Here we are simulating the pressurized fractures in the material with the smaller Young's modulus. The Poisson's ratio for both materials is taken to be the same, and the larger modulus is taken as twice that of the smaller, $E_2 = 2E_1$. The results of two sets of calculations are presented and compared with the results of previous calculations where there were no preexisting cracks in the medium (case 1). The geometry of the problems with existing cracks is shown in Fig. 10. Figure 10(a) shows the geometry of the problem (case 2) with one existing crack in the higher modulus material with length "a" (this fracture did not intersect the interface). The length of the pressurized crack is 2a. Figure 10(b) shows the geometry with preexisting cracks in the higher modulus material (case 3). Here the preexisting cracks are symmetrically located on either side of an extended fracture axis with an equal length of "a" and are spaced 2a apart. The length of the pressurized fracture is 2a.

Figure 11 shows the stress-intensity factor as a function of normalized distance of the fracture from the interface. This plot compares the stress-intensity factor for the two cases with preexisting cracks to case 1 (no preexisting fractures in the medium). We assumed the preexisting fractures to be perfectly slipping (no frictional stress).

These calculations show that preexisting fractures can reduce the effects of a materials properties change across an interface on the stress-intensity factor. For the preliminary geometries studied, case 3 (two preexisting fractures in the higher modulus material) showed the largest change from the base case, case 1. This brings up an important point in that when we measure mechanical properties, we normally choose an intact sample of the material. However, in many cases the bulk material has a significant amount of fractures greater than some given size. The results presented above show that the effective bulk elastic moduli are important parameters. This can present a dilemma because measurement of the effective bulk moduli can be extremely difficult.

CONTINUUM CONSIDERATIONS

Because we are still working in the plane, we find the "global interpolation" methods described in previous reports to be operationally more facile than local methods. Thus, the formulation of the present problems does not differ very much from that done previously,[6] which involved only the extension of the Gauss-Chebyshev method to solve problems in which a crack is tilted with respect to other cracks or an interface. Specifically, we start again with the familiar integral equation

$$\overset{(\alpha i)}{\sigma}(\underline{x}) = \int_{S_j} \overset{(\alpha\beta ij)}{\Gamma}(\underline{x}, \underline{t})\ \mu\ \overset{(\beta j)}{(\underline{t})}\, ds \quad . \tag{1}$$

The influence function $\overset{(\alpha\beta ij)}{\Gamma}(\underline{x}, \underline{t})$, for the region in question, gives the α component of stress on surface i as a result of a dislocation of unit magnitude in the β direction on surface j. We represent S_j by the function $\underline{t}(\xi)$ and S_i by $\underline{x}(\eta)$, where ξ and η are as shown in Fig. 12. Equation (1) then becomes

$$\overset{(\alpha i)}{\sigma}[\underline{x}(\eta)] = \int_{-1}^{1} \overset{(\alpha\beta ij)}{\Gamma}[\underline{x}(\eta), \underline{t}(\xi)]\ \mu\ \overset{(\beta j)}{[\underline{t}(\xi)]}\ E_j\, d\xi \quad , \tag{2a}$$

where

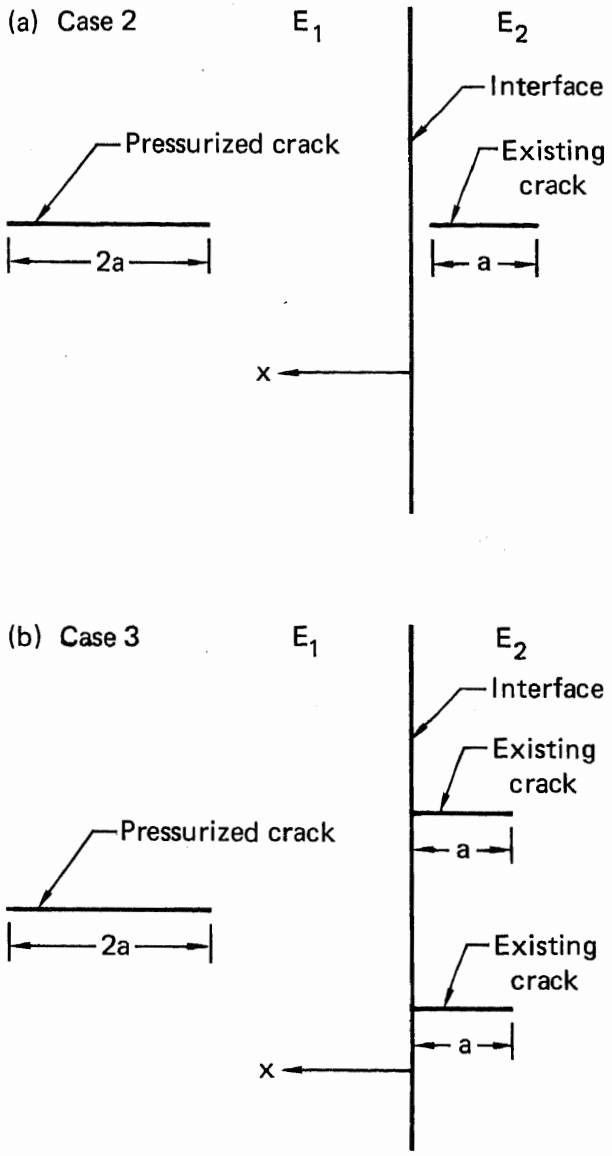

Fig. 10. Geometries of the problems for a pressurized fracture near an interface with (a) one fracture across the interface in the higher modulus material (case 2) and (b) two fractures across the interface in the higher modulus material (case 3).

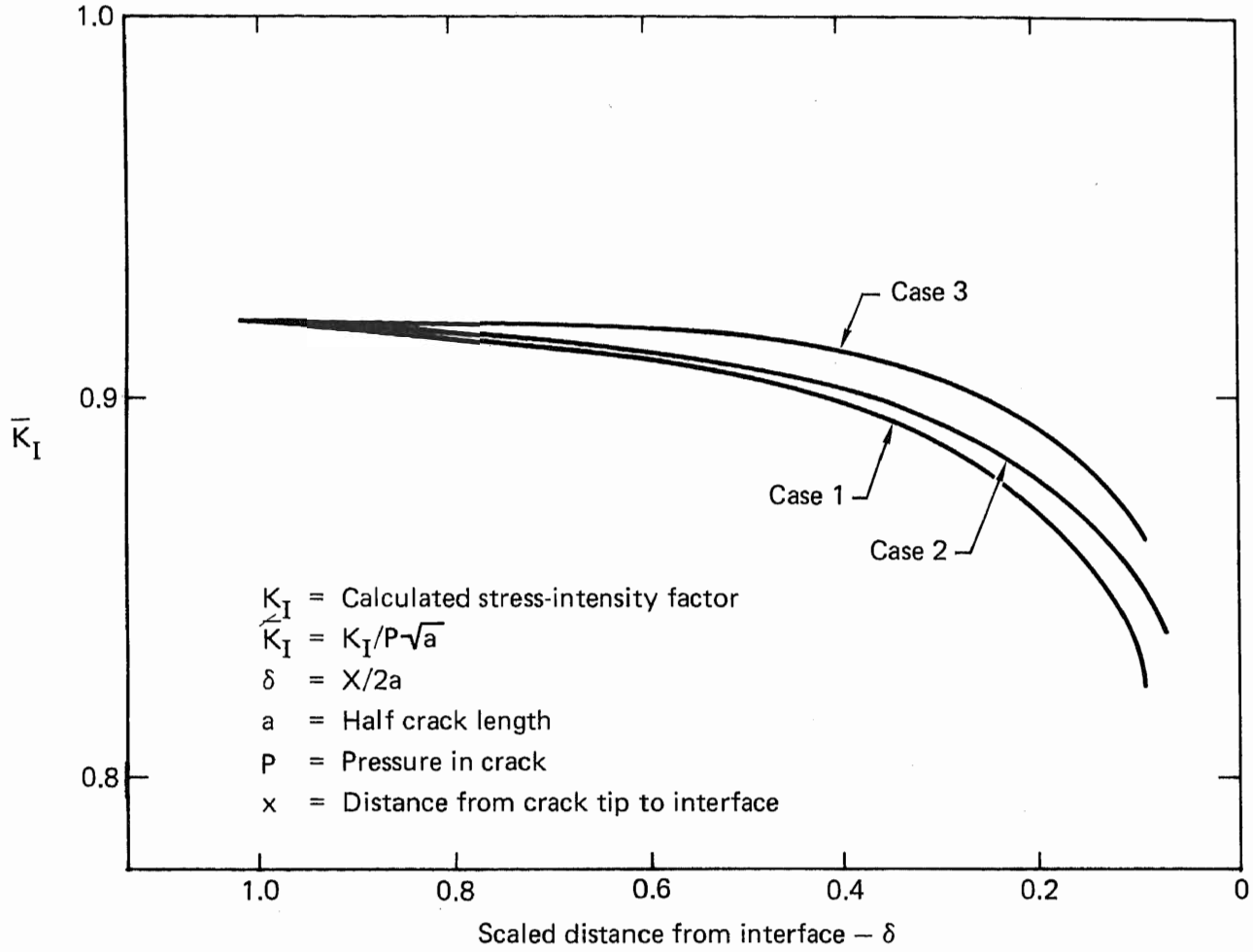

Fig. 11. Normalized Mode I stress-intensity factor as a function of scaled distances from the interface for no preexisting fractures near the interface (case 1) and with preexisting fractures near the interface (case 1) and with preexisting fractures (cases 2 and 3).

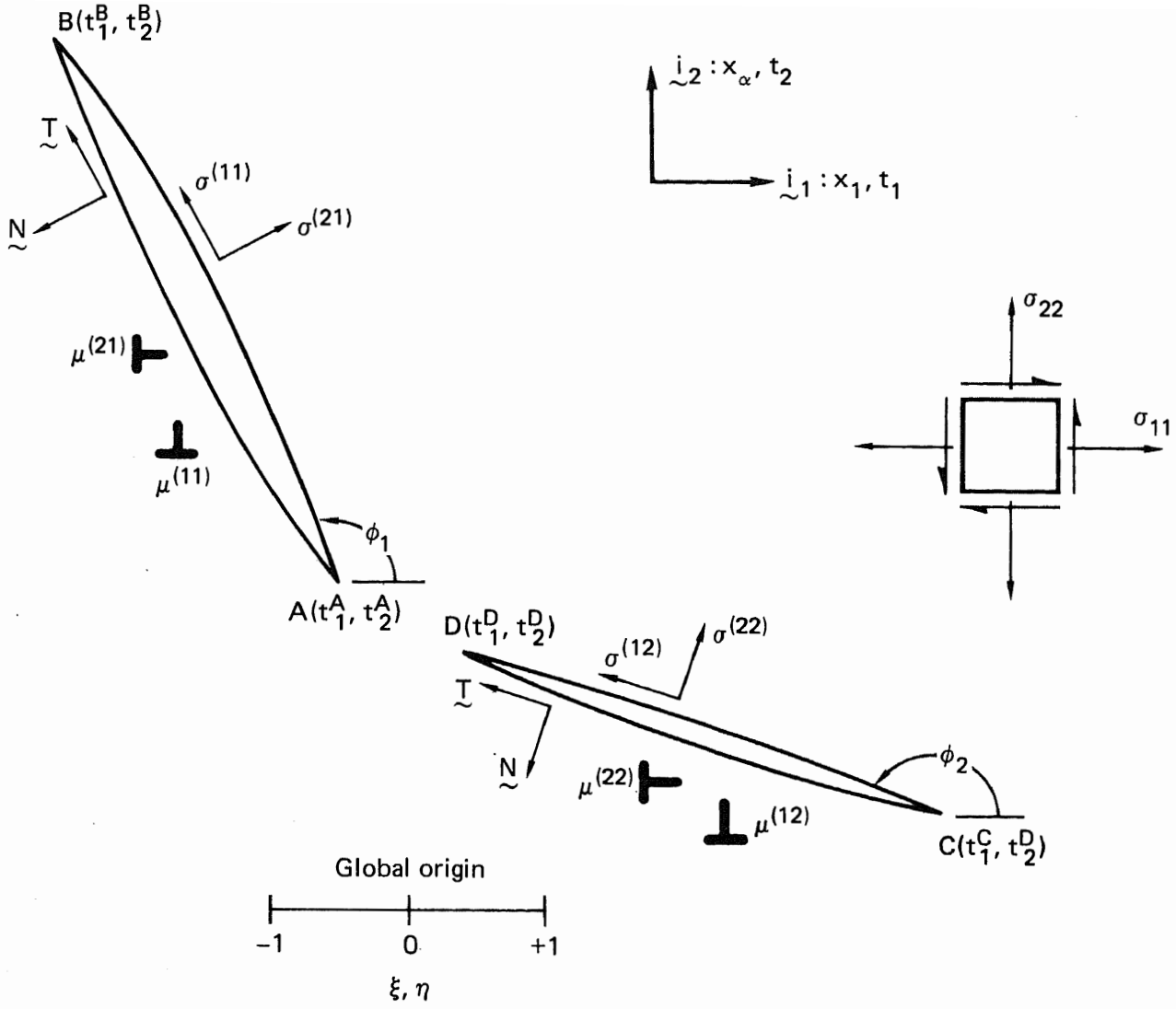

Fig. 12. Diagram showing coordinates and angles needed to formulate the general two-dimensional crack problem for numerical solution by the Gauss-Chebyshev scheme.

$$E_j = \left[\frac{d\underline{t}}{d\xi} \cdot \frac{d\underline{t}}{d\xi} \right]^{1/2} \quad . \tag{2b}$$

Note that the directions α and β refer to different coordinate systems. The directions corresponding to $\alpha = 1$ and $\alpha = 2$ are tangent and normal to S_i, while $\beta = 1$ and $\beta = 2$ correspond to the global $\underline{i}_1$ and $\underline{i}_2$ (x_1 and x_2) directions. Thus, the stress in the global system ($\sigma_{11}, \sigma_{12}, \sigma_{22}$) must be transformed to compute $\Gamma^{(\alpha\beta ij)}(\underline{x}, \underline{t})$:

$$\sigma^{(1i)} = -\tfrac{1}{2}(\sigma_{11} - \sigma_{22}) \sin(2\varphi i + \pi) + \sigma_{12} \cos(2\varphi i + \pi) \tag{2c}$$

$$\sigma^{(2i)} = \tfrac{1}{2}(\sigma_{11} + \sigma_{22}) + \tfrac{1}{2}(\sigma_{11} - \sigma_{22}) \cos(2\varphi i + \pi) + \sigma_{12} \sin(2\varphi i + \pi) \; . \tag{2d}$$

In the branched and blunted crack problems described here, we deal with two straight intersecting cracks. Thus, for S_1,

$$\begin{Bmatrix} \underline{x}(\eta) \\ \underline{t}(\xi) \end{Bmatrix} = \tfrac{1}{2}\left[t_1^B \left(1 - \begin{Bmatrix} \eta \\ \xi \end{Bmatrix}\right) + t_1^A \left(1 + \begin{Bmatrix} \eta \\ \xi \end{Bmatrix}\right) \right] \underline{i}_1 + \tfrac{1}{2}\left[t_2^B \left(1 - \begin{Bmatrix} \eta \\ \beta \end{Bmatrix}\right) + t_2^A \left(1 + \begin{Bmatrix} \eta \\ \xi \end{Bmatrix}\right) \right] \underline{i}_2 \tag{3a}$$

$$E_1 = \tfrac{1}{2}\left[(t_1^B - t_1^A)^2 + (t_2^B - t_1^A)^2 \right]^{1/2} \; ; \tag{3b}$$

for S_2,

$$\begin{Bmatrix} \underline{x}(\eta) \\ \underline{t}(\xi) \end{Bmatrix} = \tfrac{1}{2}\left[t_1^D \left(1 - \begin{Bmatrix} \eta \\ \xi \end{Bmatrix}\right) + t_1^C \left(1 + \begin{Bmatrix} \eta \\ \xi \end{Bmatrix}\right) \right] \underline{i}_1 + \tfrac{1}{2}\left[t_2^D \left(1 - \begin{Bmatrix} \eta \\ \xi \end{Bmatrix}\right) + t_2^C \left(1 + \begin{Bmatrix} \eta \\ \xi \end{Bmatrix}\right) \right] i_2 \tag{3c}$$

$$E_2 = \tfrac{1}{2}\left[(t_1^D - t_1^C)^2 + (t_2^D - t_2^C)^{2\,1/2} \right] . \tag{3d}$$

We solve equation (2a) by the Gauss-Chebyshev method. First, we reexpress the dislocation densities

$$\mu^{(\beta j)}[\underline{t}(\xi)] = \frac{F^{(\beta j)}[\underline{t}(\xi)]}{\sqrt{1 - \xi^2}} \; ; \tag{4}$$

then we define discrete points ξ_k and η_r:

$$\xi_k = \cos[(2k - 1)\pi/2N_i] \qquad k = 1, \ldots, N_i \tag{5a}$$

$$\eta_r = \cos[\pi r/(N_i - 1)] \qquad r = 1, \ldots, N_i - 1 \; . \tag{5b}$$

Equation (2a) may then be rewritten

$$\sigma^{(\alpha i)}[\underline{x}(\eta_r)] = \frac{\pi}{N_j} \sum_{1k=1}^{N_j} \left[\Gamma^{(\alpha\beta ij)}[\underline{x}(\eta_r), \underline{t}(\xi_k)] \; E_j \right] F^{(\beta j)}[\underline{t}(\xi_k)] \tag{6}$$

In the microcrack problem, $\alpha = \beta = 1$, and two more equations ("closure conditions") are needed to solve Eq. (6); namely

$$\int_{-1}^{1} \mu\,[\underline{t}(\xi)]\ \mathrm{Ej}\,\mathrm{d}\xi = \frac{\pi}{\mathrm{Nj}} \sum_{k=1}^{\mathrm{Nj}} F^{(ij)}\,[\underline{t}(\xi_k)]\mathrm{Ej} = 0 \quad . \tag{7}$$

To solve the branched and blunted crack problems, four equations are needed to complete the system (6); these arise from two closure conditions

$$\sum_{j=1}^{\alpha} \int_{-1}^{1} \mu\,[\underline{t}(\xi)]\mathrm{Ej}\,\mathrm{d}\xi = \sum_{j=1}^{\alpha} \frac{\pi}{\mathrm{Nj}} \sum_{k=1}^{\mathrm{Nj}} \mathrm{Ej}\ F^{(\beta j)}[\underline{t}(\xi_k)] = 0, \quad \beta = 1,2 \quad , \tag{8}$$

and two "matching conditions" which relate the values of $F^{(\beta 1)}$ and $F^{(\beta 2)}$ at the points $\underline{t}(\xi_k)$ nearest the intersection of the two cracks. For the results presented here we have chosen between two types of matching conditions.

For the branched crack problem, we first employed the matching condition given by Gupta[8] for comparison with his work and that of Lo,[9] which deal with cracks loaded in uniaxial tension. This takes the form

$$F^{(11)}_{(0)}\ A + F^{(22)}_{(0)}\ [C\ \sin\theta - B\ \cos\theta] - F^{(12)}_{(0)}\ [C\ \cos\theta + B\ \sin\theta] = 0 \ , \tag{9a}$$

$$F^{(21)}_{(0)}\ D + F^{(22)}_{(0)}\ [F\ \sin\theta - E\ \cos\theta] - F^{(12)}_{(0)}\ [F\ \cos\theta + E\ \sin\theta] = 0 \ , \tag{9b}$$

where

$$A = \sqrt{\frac{l_1}{l_2}}\ \cos(\pi\alpha) \ , \tag{9c}$$

$$B = (2 - \alpha)\ \sin\theta\ \cos[(1 - \alpha)\theta] \ , \tag{9d}$$

$$C = \cos(\alpha\theta) - \alpha\ \sin\theta\ \sin[(1 - \alpha)\theta] \ , \tag{9e}$$

$$D = \sqrt{\frac{l_1}{l_2}}\ \cos(\pi\alpha) \ , \tag{9f}$$

$$E = \cos[(2 - \alpha)\theta] + \alpha\ \sin\theta\ \sin[(1 - \alpha)\theta] \ , \tag{9g}$$

$$F = -\alpha\ \theta\ \cos[(1 - \alpha)\theta] \ . \tag{9h}$$

The coefficient α is derived by solving the equation

$$(1 - \alpha)^2\ \sin^2\theta - \sin^2[(1 - \alpha)(\pi + |\theta|)] = 0 \ . \tag{9i}$$

We obtain perfect agreement with the results in Ref. 8, thus verifying our somewhat novel formulation. We have also been able to construct physically reasonable results for other loading conditions (specifically internal pressure on both cracks), as described later, by using specially constructed (e.g. symmetry) arguments, but we are still seeking a general formula to adequately represent these matching conditions for arbitrary loading.

The blunted crack results presented in this report were obtained using matching conditions which represent the requirement that there be no logarithmic stress singularity in the material near the intersection of the two cracks; thus, the jumps in the dislocation density must vanish:

$$\mu_{(0)}^{(11)} + \mu_{(0+)}^{(22)} - \mu_{(0-)}^{(22)} = 0 \tag{10a}$$

$$\mu_{(0)}^{(21)} - \mu_{(0+)}^{(12)} - \mu_{(0-)}^{(12)} = 0 \ . \tag{10b}$$

Once Eq. (6) has been solved, we transform F from global Cartesian coordinates to local normal and tangential coordinates

$$F^{(Tj)}(\underline{t}) = F^{(1j)}(\underline{t}) \cos\varphi_j - F^{(\alpha j)}(\underline{t}) \sin\varphi_j \tag{11a}$$

$$F^{(Nj)} = F^{(1j)}(\underline{t}) \sin\varphi_j + F^{(\alpha j)}(\underline{t}) \cos\varphi_j \ , \tag{11b}$$

then we compute the stress-intensity factors from the relations (similar to those given by Cleary[10])

$$K^{(j)} = \frac{2G}{1-\nu}\sqrt{\frac{\pi l_j}{2}}\, F^{(j)} \ . \tag{12}$$

MICROCRACK PROBLEM

We first solved the microcrack problem with a unit-positive normal load on the hydraulic fracture and no load on the microcrack so as to obtain the stress-intensity factor at the tip of the unloaded microcrack, K_{Iu} [see Fig. 13(a) for geometry of this problem]. The problem was then solved for the converse crack loading to obtain the stress-intensity factor at the tip of the loaded microcrack, K_{II}. By superposition we can write the expression for K_I at the microcrack tip for the case where the hydraulic fracture is subjected to fracture fluid pressure P_0 and confining stress $-\sigma_M$ and the microcrack to $-\sigma_M$ alone

$$K_I = (P_0 - \sigma_M)K_{Iu} - \sigma_M K_{II} \ . \tag{13}$$

From this we can deduce that for K_I to be positive, the ratio of fracture fluid pressure to confining stress must exceed

$$\left(\frac{P_0}{\sigma_M}\right)_c = \frac{K_{II}}{K_{Iu}} + 1 \ . \tag{14}$$

The effects of geometric and material parameters on $(P_0/\sigma_M)_c$ are shown in Figs. 14 and 15. Of special interest is the fact that the capability to actually open the microcrack is not strongly affected by the size of the microcrack. It is also apparent that the proximity of the hydraulic fracture to the interface is more important than that of the microcrack. The ratio of shear moduli for the strata is also an important factor.

Figure 14 shows that it is possible to produce a positive K_I at the tip of a microcrack without having a fracture fluid pressure excessively above the confining stress. For example, a fracture fluid pressure of $1.4\sigma_M$ in a 30-ft hydraulic fracture 1.5 ft from an interface (with a shear modulus ratio of 2) can produce a positive K_I at the tip of a 3.5-in. microcrack 3.5 in. from the interface. Figure 15 shows that if the same hydraulic fracture were instead 4 in. from the interface (still not strongly under the influence of the

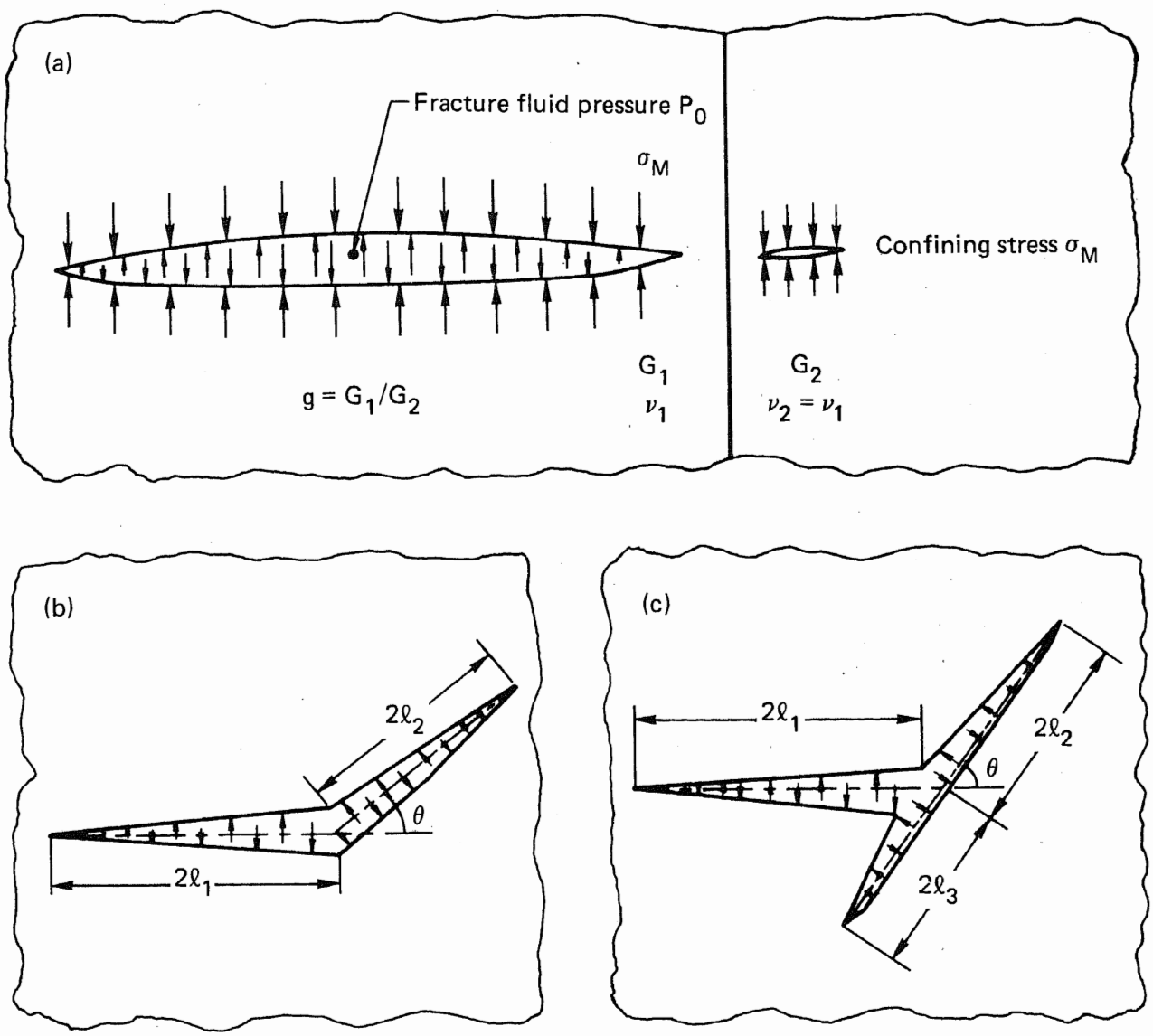

Fig. 13. (a) Diagram of the microcracks problem. We must determine the fracture fluid pressure required to cause a positive stress-intensity factor at the near-interface tip of the microcracks for given microcracks and hydraulic fracture lengths, distances from the interface and relative shear moduli; (b) diagram of the branched crack problem; (c) diagram of the blunted crack problem.

elasticity barrier), the same fracture fluid pressure would produce a positive stress-intensity factor at the top of a 3.5-in. microcrack as far as 3 ft beyond the interface. Statistically,* this provides a higher probability of finding enough microcracks and damage to back-propagate ahead of the major fracture.

We conclude that microcracks are significant factors influencing the containment of hydraulic fractures in shallow, soft strata. It is in these situations—where the lateral confining stresses are small compared to the fracture fluid pressures required for hydraulic fracture propagation—that microcracks in a stiff adjacent stratum can be easily induced to break through the interface and link up with the hydraulic fracture. Thus, the hydraulic fracture can overcome the elasticity barrier presented by the stiff stratum and thereby break out of the pay zone. At greater depths, we expect the hydraulic fracture to be more readily contained in the pay zone by the

*Note that our conclusions here need very little modification in discussing the three-dimensional character of the real field operation.

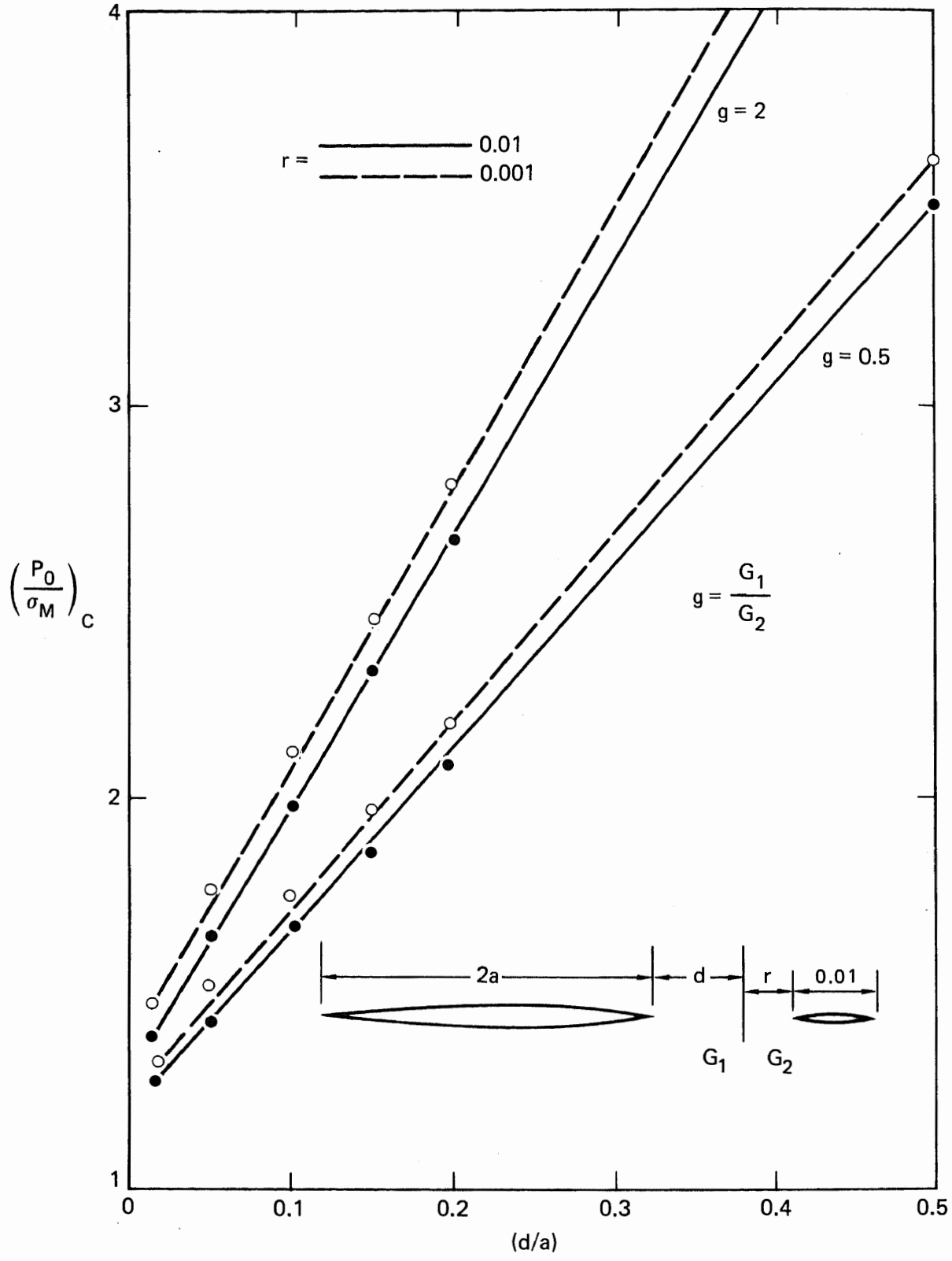

Fig. 14. Plot of $(\rho_l/\sigma_m)_c$ as a function of the distance from the tip of the hydraulic fracture to the interface for the microcrack problem.

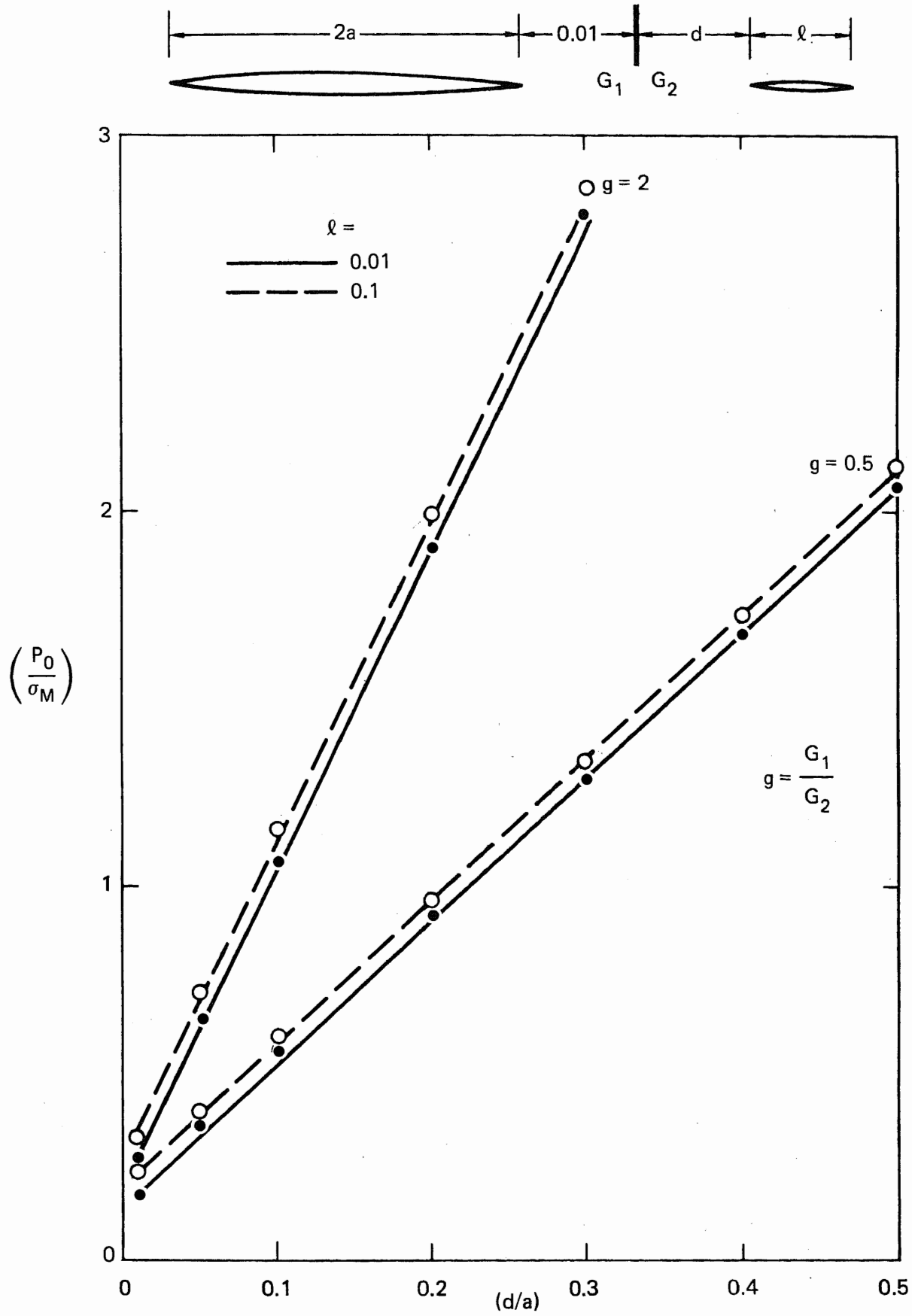

Fig. 15. Plot of $(\rho_0/\sigma_m)_c$ as a function of distance from the tip of the microcrack to the interface for the microcrack problem.

elasticity barrier because the fracture fluid pressure required for propagation is then such that $(P_0-\sigma_M)/\sigma_M$ can be too small for the above mechanism to operate.

BRANCHED CRACK PROBLEM

To validate our formulation of the general two-dimensional homogeneous medium, we tested our computer program on the case of a branched crack in an infinite plane subjected to uniaxial tension. [The geometry of this problem is shown in Fig. 13(b)]. The results are in excellent agreement with those of Gupta[8] ($K_I/\sqrt{\pi a} = 1.0873$ vs 1.0852, 0.7463 vs 0.7450, 0.3900 vs 0.3880 for $\theta = 30, 45, 60$ deg, respectively), who also uses a formulation based on dislocations in the plane, and are in fair agreement with Lo[9].

For the internally pressurized pair of cracks, a plot of K_I and K_{II} as a function of the branching angle θ is shown in Fig. 16. We attribute the decrease of K_I with increasing θ to the decreasing portion of the total crack length subject to loading in one of the two normal directions. Likewise, the increase in K_{II} is related to the increasing shear component on S_i of the fracture fluid pressure acting on S_j. If effective length were the only factor affecting K_I, we would expect the decrease to be very roughly described by

$$K_I = \sqrt{\frac{\ell}{\alpha}(1 + \cos\theta)} \cdot \tag{15}$$

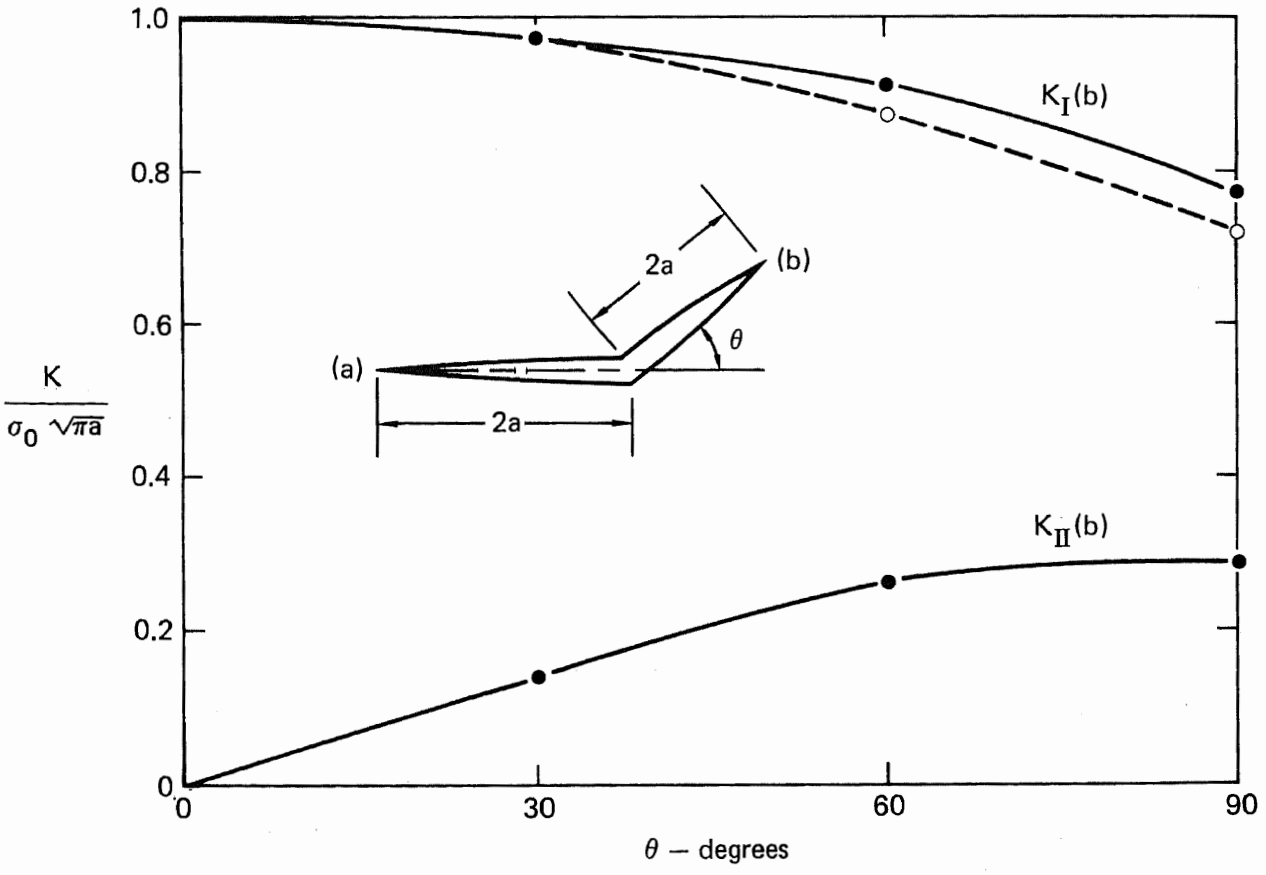

Fig. 16. Plot of stress-intensity factors as function of branching angle for the branched crack problem. The dashed line is a plot of Eq. (15)—a rough preliminary estimate of the expected behavior of $K_I(b)$.

Equation (15) is plotted as a dashed line in Fig. 16. For small values of θ, the agreement between the computed K_I and that predicted by Eq. (16) is quite good, but at greater angles we see that K_I does not drop as far as we would expect. It is likely that with increasing θ, the decrease of K_I is moderated by the tendency of one surface to partly influence the other as if it were a free surface.

We take the small drop in K_I even up to 90-deg angles of branching to indicate that a hydraulic fracture should not exhibit great resistance to branching in the presence of material- or stress-field barriers or irregularities. Thus, it is possible that hydraulic fractures will in some cases be contained by branching away from interfaces where high resistance to continued straight propagation is experienced.

BLUNTED CRACK PROBLEM

The results of our investigation of the behavior of blunted cracks are shown in Fig. 17 [see Fig. 13(c) for the geometry of the problem]. The essential feature is the behavior of the opening mode stress-intensity factors at the tips of both the primary and secondary cracks, namely, $K_I(a)$ and $K_I(b)$, respectively. We note that the elevation of $K_I(a)$ with increased blunting reverses as expected when the length of the secondary crack exceeds that of the primary crack, but that with increasing secondary crack length, $K_I(b)$ rises much more strongly than we had anticipated.

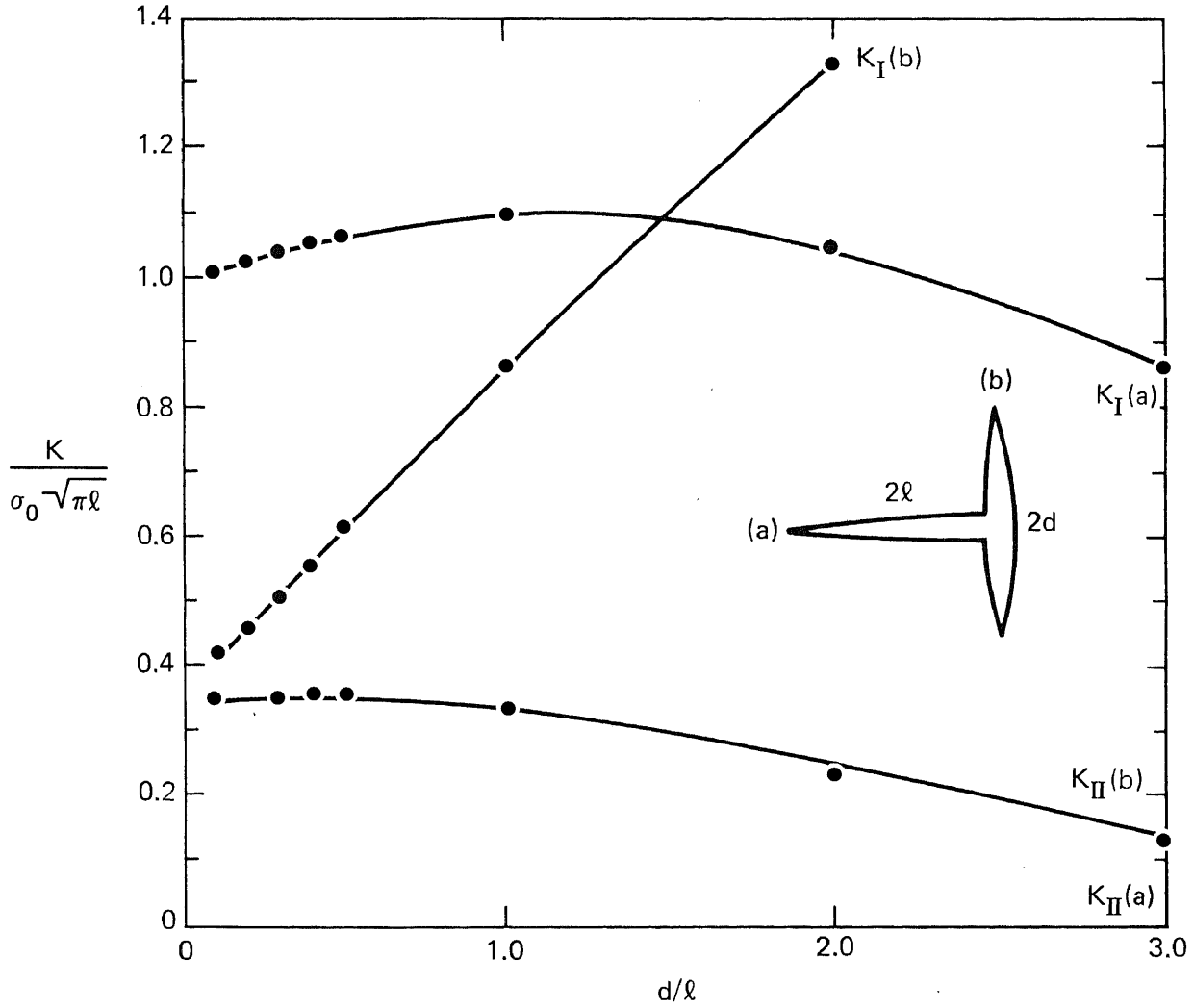

Fig. 17. Plot of stress intensity factors vs size of secondary crack for the blunted crack problem.

The initial rise of $K_I(a)$ is probably caused by the development of a free surface effect like that encountered in the branched crack problem: the secondary crack offers much less resistance to the opening of the primary crack than would the unbroken material. When the secondary crack exceeds the primary in length, the effect of the fluid pressure in the secondary crack overwhelms the free surface effect by producing a compressive stress on the prospective locus of the primary crack, thus decreasing $K_I(a)$, and thus dominating its further behavior.

In the absence of the primary crack, $K_I(b)$ would increase as $\sqrt{d/\ell}$. We find this to be the case for large d/ℓ. The relative behavior of $K_I(a)$ and $K_I(b)$ is substantial evidence that once the secondary crack becomes long enough, propagation of the primary crack away from the secondary crack will be virtually stopped. Thus, while blunting may result in containment of a hydraulic fracture, it may also inhibit propagation away from an interface.

LABORATORY EXPERIMENTS

FRICTIONAL INTERFACE

Studies are continuing to determine the important parameters that control whether hydraulically driven cracks will cross an unbonded interface in a rock. When the same rock is on both sides of the interface we have found that the normal stress across the interface and, in the case of Nugget sandstone, the texture of the interface are important. In the case of Indiana limestone we have found that a crack will cross more easily, i.e., at a lower normal stress across the interface, from dry to water-saturated limestone than from dry to dry limestone. Tests have shown that the tensile strength of water-saturated limestone is about 40% that of dry limestone while the shear strength is about the same. At present we are uncertain as to why our results show a change in tensile strength with saturation but no change in shear strength. We plan more tests and analyses to resolve these results. In addition, we plan tests to measure the frictional shear-strength characteristics of unbonded interfaces between rocks of the same type and of different types. To perform these tests we have constructed the apparatus shown schematically in Fig. 18. A 2-in. cube of rock is held between two $2 \times 4 \times 4$-in. prismatic blocks of the same material, which may or may not be of the same material as the 2-in. cube. A hydraulically driven ram applies normal stress across the two interfaces. We determine the magnitude of the stress load by measuring the hydraulic fluid pressure driving the ram. A vertical ram applies a vertical driving force that moves the center cube downward against the frictional force caused by the two outer prisms. This driving force is measured by a load cell. The static coefficient of friction or static shear strength can then be computed from the magnitude of vertical force necessary to initiate slippage as a function of applied normal load. Both the driving force and the normal interface load are monitored as a function of time and recorded on chart recorders. This symmetrical system for friction measurements is a well known technique and has been used by others.[11, 12]

EFFECT OF PRINCIPAL STRESS MAGNITUDES ON HYDROFRACTURING ORIENTATION

We have continued our experiments to establish the effects of principal stress magnitudes on hydrofracturing orientation to obtain the following results:

- Establish the effect of the vertical stress on the direction and inclination of hydrofractures in the vicinity of the borehole wall for a set condition of horizontal stresses.
- Determine the minimum difference between the two principal horizontal stresses for which hydrofractures cease to be randomly oriented and become aligned with the direction of maximum horizontal stress.

We conducted this study in the laboratory using prismatic specimens $5 \times 5 \times 7$ in. high. We applied three independent and mutually perpendicular loads to the faces of the specimens, simulating the three principal *in situ* stresses. We induced hydrofractures by hydraulically pressurizing a vertical borehole in the center of the specimen.

In prior laboratory work, we tested specimens of Montello granite to determine how the vertical stress and the horizontal stress differential affect hydrofracture orientation. In all tests except one, we initiated fractures vertically at the borehole wall. In those tests in which the horizontal principal stresses were held constant at a ratio

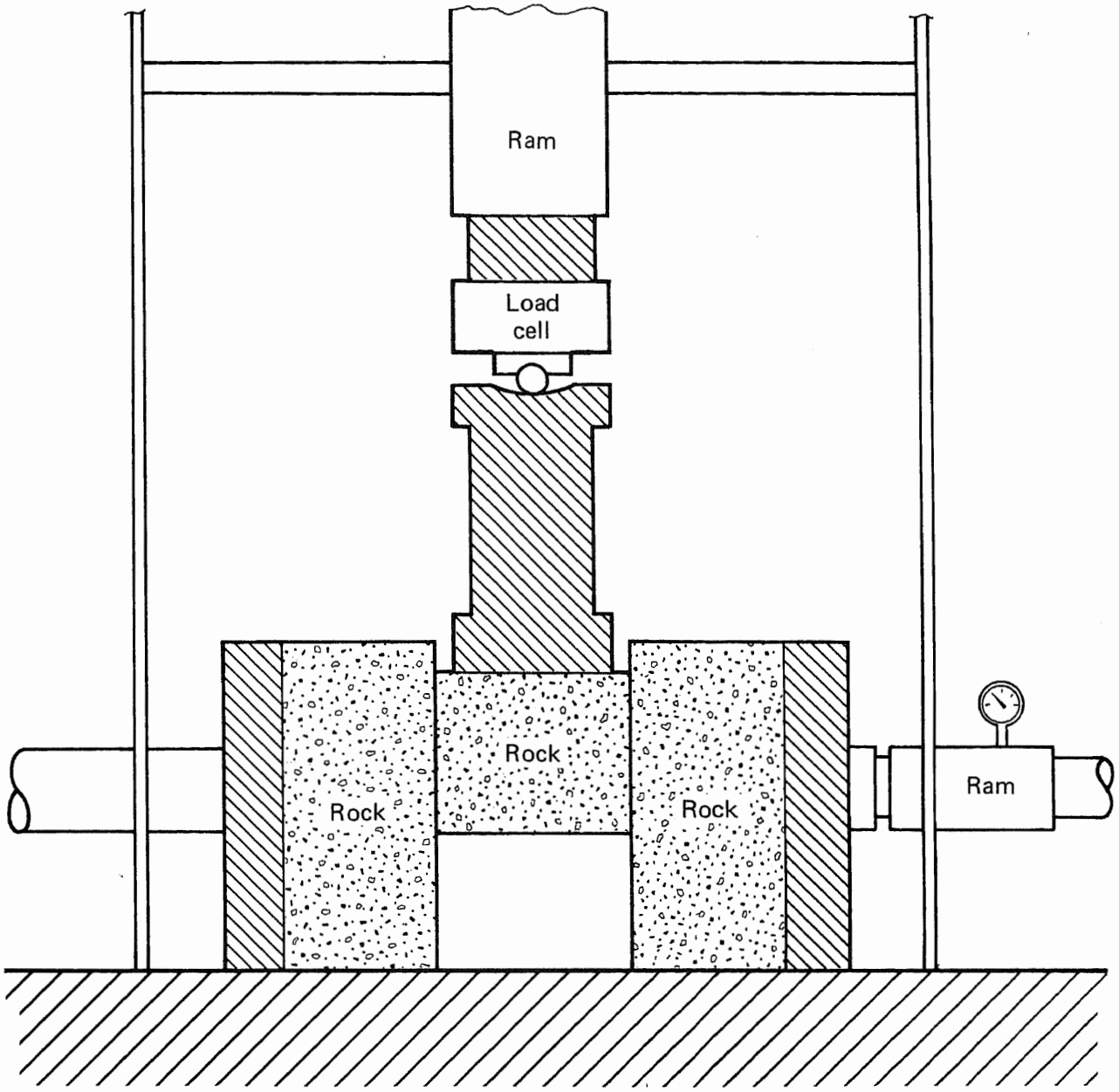

Fig. 18. Apparatus for friction measurements.

of 2:1, the vertical fractures were always perpendicular to the direction of σ_{Hmin}. For ratios of σ_{Hmin}/σ_V larger than 1:1, the initially vertical fractures turned away from the borehole to become horizontal before emerging at the face of the specimen. For ratios of σ_{Hmin}/σ_V smaller than 1:1, the fracture stayed vertical throughout the specimen.

When the vertical stress was kept constant from test to test, the resulting hydrofractures were perpendicular to σ_{Hmin} as long as σ_{Hmax} was 2000 psi and σ_{Hmin} was any value between 0 and 1900 psi. For $\sigma_{Hmax} - \sigma_{Hmin} < 100$ psi, the orientation of vertical hydrofractures was unpredictable.

The objective of this laboratory research was to repeat the tests in another rock type to assess the generality of the findings in Montello granite. For this we chose Dresser basalt.

Dresser basalt is found in Dresser, Wisconsin, and has been geologically classified as either an altered gabbro or an altered basalt, but the latter term is most commonly used. It is a very strong, coarse-grained rock with

low porosity and permeability. It is very nearly isotropic and some of its mechanical properties, as determined by U.S. Bureau of Mines,[14] are as follows:

- Uniaxial compressive strength, psi 64,000.
- Uniaxial tensile strength, psi 3,200.
- Porosity, % 0.29.
- Permeability, mD 0.1.
- Young's modulus, psi $12.5 + 10^6$.
- Poisson's ratio 0.26.

The rock specimens used in this series of tests were 5 × 5 × 7-in. prismatic blocks. The specimens were loaded horizontally using flat jacks. Borehole pressure was raised using a constant flow rate. The apparatus and testing procedure are detailed in Ref. 13.

Acoustic Emission

In most of the tests, we monitored and recorded the acoustic emission (AE) during borehole pressurization. We suspected that such emission may be generated by initial microfracturing, leading to the eventual hydrofracturing of the rock. The AE recording does not suggest that such activity occurred during these tests. The only AE observed was that emanated by the hydrofracturing itself (Fig. 19).

Effect of Horizontal Stress on Hydrofracture Orientation

We tested twenty specimens of Dresser basalt to verify the effect of horizontal stresses on the inclination and direction of hydrofractures. The magnitudes of the largest horizontal stress σ_{Hmax} and the vertical stress σ_V were kept at 2000 and 4000 psi, respectively. The least horizontal stress σ_{Hmin} was varied between 650 and 2000 psi. Table 1 gives the experimental details and results.

In all tests, hydrofractures were initiated vertically at the borehole. They extended in a direction perfectly perpendicular to σ_{Hmin} so long as $\sigma_{Hmax} - \sigma_{Hmin} > 300$ psi. In most of the tests, σ_{Hmin} was kept within 300 psi from σ_{Hmax}. For σ_{Hmin} values of 1700 and 1750 psi (giving a horizontal stress differential of 300 and 250 psi, respectively) the vertical hydrofracture deviation from perpendicular to $_{Hmin}$ was only 10 deg. However at $\sigma_{Hmin} = 1800$ psi ($\sigma_{Hmax} - \sigma_{Hmin} = 200$ psi), the three tests conducted yielded three different orientations for the resulting vertical hydrofractures (45, 75 and 90 deg with respect to σ_{Hmin}), implying that local imperfections in the rock structure

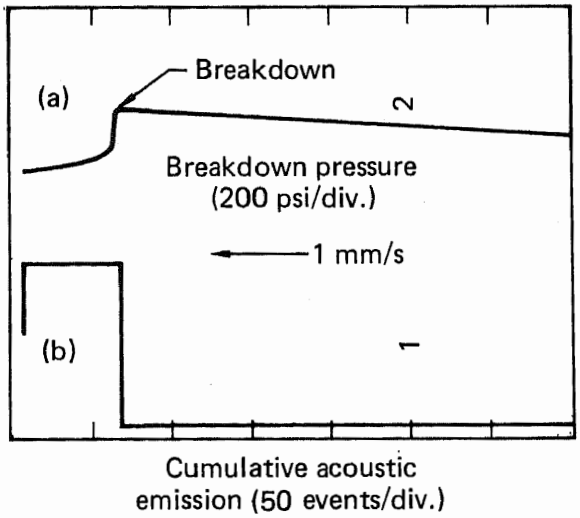

Fig. 19. (a) Hydrofracturing pressure vs time; (b) cumulation acoustic emission vs time.

Table 1. Effect of horizontal stresses on hydrofracture orientation and breakdown pressure in Dresser basalt (σ_{Hmax} = 2000 psi, and vertical stress = 4000 psi).

Specimen No.	Horizontal stress (σ_{Hmin}), psi	Breakdown pressure, psi	Vertical hydrofracture orientation with respect to σ_{Hmin}, deg
202	650	4700	90
101	1000	4600	90
302	1000	4850	90[a]
102	1500	4400	90[a]
301	1500	3800	90[a]
502	1700	5050	80
503	1750	2700	80
404	1800	4800	45
303	1800	5000	90[a]
203	1800	4500	75
403	1850	4700	75
504	1850	4300	80
402	1900	4450	70
304	1900	4700	80
103	1900	3700	55
602	1900	4150	70
204	1950	3400	75
401	1975	4100	90
104	2000	5600	60

[a]Recorded in inches instead of degrees

become as effective as the stress differential in this range. This trend continues as σ_{Hmin} approaches σ_{Hmax} in magnitude, but the fracture is seldom more than 20 deg away from its expected perpendicularity to σ_{Hmin} direction.

In general, although deviations in hydrofracture direction from the expected 90 deg to σ_{Hmin} begin at a considerably larger horizontal stress differential than in the Montello granite (300 psi vs 75 psi), they are almost always small and restricted to less than 25 deg.

Similarly to Montello granite, the breakdown pressures in Dresser basalt appear to be rather insensitive to variations in σ_{Hmin}, contrary to theoretical expectations. We recommend an investigation of these experimental results and their relationship to theoretically expected values.

EFFECT OF VERTICAL STRESS ON HYDROFRACTURE ORIENTATION

We subjected specimens of Dresser Basalt to different vertical stresses while keeping the horizontal stress field constant (σ_{Hmin} = 2,000 psi, σ_{Hmax} = 4,000 psi). We attempted hydrofracturing for values of σ_V ranging from 100 to 5,000 psi. Table 2 gives the experimental details and results.

In a few cases of low σ_V we did not observe any vertical hydrofracture. Rather, horizontal hydrofractures appeared to extend from the borehole wall to the outer face of the specimens. In the great majority of the cases, however, vertical fractures perpendicular to σ_{Hmin} initiated at the borehole wall. For values of σ_V less than 750 psi, the vertical fractures became horizontal or subhorizontal before reaching the outside face of the specimen. For higher values of σ_V, fractures remained vertical throughout the specimen. These results are similar to those obtained for the Montello granite and appear to be general in character.

Theoretically, the value of the breakdown pressure should have stayed constant as the horizontal stress field was not changed from test to test. In practice, the breakdown pressure varied between 3400 and 5050 psi for

Table 2. Effect of vertical stress on hydrofracture orientation and breakdown pressure in Dresser basalt (σ_{Hmin} = 2,000 psi; σ_{Hmax} = 4,000 psi).

Specimen No.	Vertical stress, psi	σ_{Hmin}/σ_V	Breakdown pressure, psi	Hydrofracture[a]
5-4	100	20	2800	A
1-1	100	20	3950	A
1-2	200	10	4200	B
4-1	200	10	4700	C
1-3	300	20/3	4850	B
5-2	300	20/3	3400	C
2-1	500	4	4600	B
3-1	500	4	4350	C
5-3	500	4	3800	C
2-2	750	8/3	3600	B
5-1	750	8/3	3650	D
2-3	1000	2	5050	D
3-3	2000	1	4450	D
4-2	2000	1	4400	D
4-3	3000	2/3	4800	D
4-4	4000	1/2	4850	D
4-5	5000	2/5	4600	D

[a] A — Fracture unclear.
B — Horizontal to subhorizontal hydrofracture.
C — Vertical hydrofracture perpendicular to σ_{Hmin} at the borehole wall, turned into horizontal or subhorizontal as fracture approaches the face of the specimen.
D — Vertical hydrofracture perpendicular to σ_{Hmin}.

those specimens where a vertical hydrofracture was initiated. However, the average value was 4370 psi with a standard deviation of only 12%.

The two tests conducted in Dresser basalt served to verify the results previously obtained in Montello granite. We found that in massive igneous rocks hydrofractures are vertical and oriented perpendicular to the least horizontal compressive stress σ_{Hmin} if $\sigma_V \geqq \sigma_{Hmin}$ and if $\sigma_{Hmax} - \sigma_{Hmin} \geqq 200$ psi. For a horizontal stress differential less than 200 psi, the direction of the resulting vertical hydrofracture is not predictable but it tends to be within 25 deg from perfect perpendicularity to σ_{Hmin}.

When the vertical stress is smaller than σ_{Hmin}, we found that in the great majority of cases the hydrofractures initiated in the vertical plane perpendicular to σ_{Hmin} but extended along a horizontal plane perpendicular to the least principal stress.

The two rocks tested varied in details of the results as can be seen by comparing individual tests. However, the overall agreement is obvious and leaves little doubt that it is representative of most fairly isotropic massive rocks.

RESERVOIR ANALYSIS

ANALYSIS OF MOBILE'S PICEANCE CREEK UNIT WELL F 31-136

We have completed a second analysis of the data from the Mobile Research and Development Corporation's Piceance Creek Unit Well F 31-136. The previous analysis[3] used "scum", a fracture-formation resistance factor

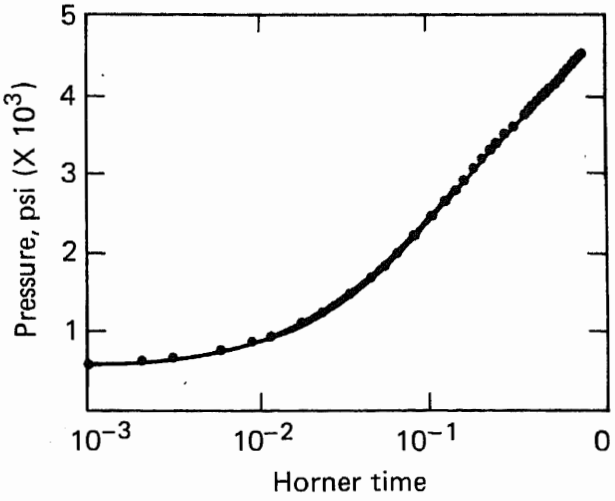

Fig. 20. Pressure buildup vs Horner time. Crosses show actual data points for the well described in text. Solid lines are results of model comparison using parameters in text. Upper line is for finite conductivity in crack and lower line is for skin damage "scum" on fracture focus.

similar to skin damage, but on the fracture faces, to fit the data. This second model did not use scum, but rather used a finite conductivity in the fracture. Figure 20 shows the good fit to the data achieved by the two models. Where there is a difference in the models, the finite conductivity fracture model shows a slightly higher pressure.

The model parameters that were used for the final fit are:

- Formation pressure, psi 4675.
- kh, mD-ft 1.12.
- $\phi L^2 h$, ft^3 9200.
- Well and fracture storage, ft^3 3350.
- C_D 1.34.
- C_f mD-ft^2 1.5.

The fracture conductivity is determined from C_D, the dimensionless fracture conductivity, where

$$C_D = \frac{k_f\, w_f\, h_f}{k\, L_f\, h} = \frac{C_f}{C_{rf}} \quad .$$

Here quantities with subscript f refer to the fracture. The other quantities are for the formation. For our value of C_f we can calculate a fracture conductivity. If we assume

$L = 100$ ft,
$h_f = 100$ ft,
$w_f = 0.05$ ft (fracture half width),

then

$k_f = 30$ md.

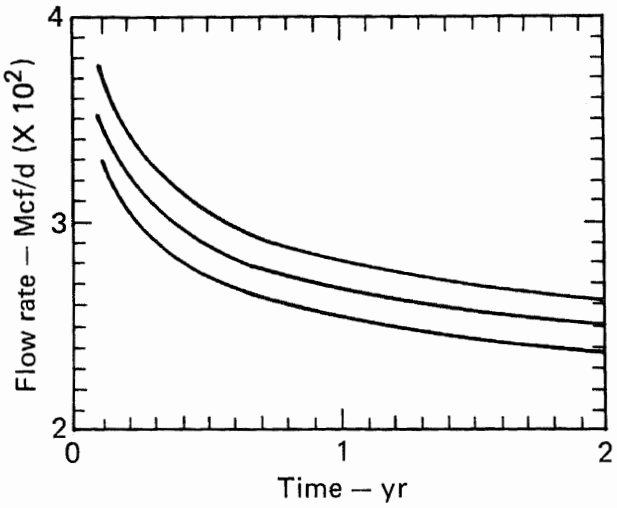

Fig. 21. Production characteristics for (1) upper line, infinite conductivity crack and no skin damage; (2) crack with "scum" skin damage in crack, middle plot and (3) lower plot, finite conductivity crack.

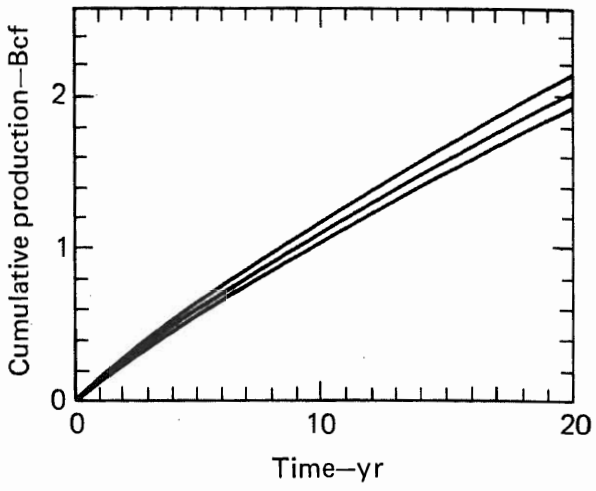

Fig. 22. Cumulative production for infinite conductivity crack, upper plot, skin damage "scum" in crack, middle plot; and finite conductivity crack, lower plot.

We also calculated the flow rate (Fig. 21) and cumulative production (Fig. 22) for 20 years. This is shown along with the results for a fracture with and without scum.

A clear fracture, scum = 0, shows the highest flow rates and production. This is followed by the scum model. The effects of finite conductivity in the fracture is to lower the curves some more. Note that while both models fit the data well, the effects on long-term production are different.

ROCK MECHANICS MEASUREMENTS

For the equation-of-state studies, we have completed the design of a high-pressure vessel for the simultaneous measurement of ultrasonic velocities in six directions on one specimen. About 80% of the fabrication work for this pressure vessel has been completed. With this vessel we can determine the elastic constant tensor of a transversely isotropic rock as a function of confining pressures up to 1.0 GPa at room temperature. This vessel can be easily altered for moderate temperature operation if such measurement would be useful to the program.

We have obtained a 15-ft core sample (2-in-diam) from the Mesaverde formation (Western Tight Gas Sand), Rio Blanco County, Colo. The specimen preparation for the equation-of-state and hot-gas permeability studies has been started.

REFERENCES

1. C. R. McKee, M. E. Hanson, and R. W. Terhune, *Permeability from Single and Multiple Detonations of Explosive Charges,* Lawrence Livermore Laboratory, Rept. UCRL-78207, Rev. 1 (1976).
2. M. E. Hanson, B. K. Crowley, and J. S. Kahn, *Massive Hydraulic Fracturing: Identification of Critical Technical Issues for Application in Increasing Gas Production in The Western United States,* Lawrence Livermore Laboratory, Rept. UCRL-51751 (1975).
3. M. E. Hanson, G. D. Anderson, R. J. Shaffer, D. N. Montan, B. Haimson, and M. P. Cleary, *LLL Gas Stimulation Program Quarterly Progress Report, January through March 1978,* Lawrence Livermore Laboratory, Rept. UCRL-50036-78-1 (1978).
4. N. R. Warpinski, D. A. Northrup, and R. A. Schmidt, *Direct Observation of Hydraulic Fracture: Behavior Near a Fracture Interface,* Sandia Laboratories, Albuquerque, New Mexico, Rept. SAND 78-1935 (1978).
5. M. E. Hanson, G. D. Anderson, R. J. Shaffer, J. R. Hearst, B. Haimson, and M. P. Cleary, *LLL Gas Stimulation Program Quarterly Progress Report April through June 1978,* Lawrence Livermore Laboratory, Rept. UCRL 50036-78-2 (1978).
6. M. E. Hanson, G. D. Anderson, R. J. Shaffer, D. O. Emerson, R. P. Swift, K. O'Banion, M. P. Cleary, B. Haimson, C. F. Knutson, and C. R. Boardman, *LLL Gas Stimulation Program Quarterly Progress Report July through September 1978,* Lawrence Livermore Laboratory, Rept. UCRL 50036-78-3 (1978).
7. S. H. Advani and H. V. S. GagaRoo, *Fracture Mechanics Investigation Associated with Coring and Hydraulic Induced Fractures,* Engineering Experiment Station Report, College of Engineering, West Virginia University, Morgantown, West Virginia (1978).
8. G. D. Gupta, "Strain Energy Release Rates for Mixed Mode Crack Problems," ASME Paper No. 76-WA/PVP-7 (1976).
9. K. K. Lo, "Analysis of Brancher Cracks," *J. of Appl. Mech. 45,* 797–802 (1978).
10. M. P. Cleary, "Moving Singularities in Elasto-Diffusive Solids with Applications to Fracture Propagation," *Int. J. Solids Structures 14,* 81–97 (1978).
11. J. C. Jaeger and N. G. W. Cook, *Fundamentals of Rock Mechanics* (John Wiley & Sons, Inc., New York, 1969).
12. E. R. Hoskins, J. C. Jaeger, and K. J. Rosengren, *Int. J. Rock Mech. Min. Sci. 5,* 143–154 (1968).
13. M. E. Hanson, R. J. Shaffer, G. D. Anderson, D. N. Montan, W. Lin, B. Haimson, and M. P. Cleary, *LLL Gas Stimulation Program Quarterly Progress Report October through December 1977,* Lawrence Livermore Laboratory, Rept. UCRL-50036-77-4 (1978).
14. W. W. Krech, F. A. Henderson, and K. E. Hjelmstad, *A Standard Rock Suite for Rapid Excavation Research,* U. S. Bureau of Mines Report of Investigation 7865 (1974).

MLD